IEEE Open Journal of the
Industrial Electronics Society

Received 20 February 2024; revised 12 April 2024; accepted 19 April 2024. Date of publication 26 April 2024;
date of current version 3 May 2024. The review of this paper was arranged by Associate Editor Chunhua Liu.

Digital Object Identifier 10.1109/OJIES.2024.3394290

HESS Management for Virtual Inertia, Frequency, and Voltage Support Through Off-Board EV Bidirectional Chargers

JHONATAN D. PAUCARA [1], JOSÉ CARLOS U. PEÑA [2], AND DAMIAN SAL Y ROSAS [3]

[1]National University of Engineering, Lima 15333, Peru
[2]Department of Electrical and Computing Engineering, Universidade Estadual de Campinas, Campinas 13083-852, Brazil
[3]LAAS-CNRS, University of Toulouse, 31031 Toulouse, France

CORRESPONDING AUTHOR: JHONATAN D. PAUCARA (e-mail: jpaucarapr@uni.pe)

This work was supported by Concytec-Prociencia by the project "Manufactura Avanzada de Estaciones de recarga rápida de vehículos eléctricos basada en Sistemas Fotovoltaicos Inteligentes [Contract N° 007-2021]."

ABSTRACT The massive integration of renewable energies into the grid using fast-response converters without inertia generates issues such as inertia reduction, temporary voltage violations, and power quality reduction. The system inertia reduction is a critical problem that could lead to grid frequency exceeding the acceptable range, resulting in undesirable load-shedding or even large-scale blackouts. To overcome these issues, the use of electric vehicle bidirectional chargers (EVBCs) implementing functionalities such as distributed virtual inertia (VI), long-term frequency support, voltage support by reactive power, and harmonics compensation, has been proposed as a possible solution. This article proposes a novel control strategy to manage a hybrid energy storage system (HESS) composed of dc-link capacitors and battery, through an isolated two-stage ac–dc converter (composed of a dual active bridge resonant type dc–dc converter cascaded to a voltage source inverter), intended for off-board EVBCs. The HESS management allows decoupling of the active power dynamic response since dc-link capacitors supply the fast dynamic response for VI support whereas the battery supplies the slower dynamic response for long-term frequency support, respectively. Hence, the VI support does not affect the battery lifetime. Simulations and experimental results are presented for a 2.5 kW prototype to validate VI, frequency-voltage support along with harmonics compensation.

INDEX TERMS Electric vehicles, off-board, bidirectional chargers, virtual inertia (VI), hybrid energy storage system (HESS), frequency support, reactive support, harmonics compensation.

I. INTRODUCTION

Electric vehicles bidirectional chargers implementing vehicle-to-grid (V2G) functionalities have been proposed as a possible solution to compensate voltage and frequency variations in distribution grids having a high integration of renewable energies [1], [2]. Most renewable energy systems are connected to the grid through inertialess power electronics converters, leading to a decrease in the overall system inertia and consequently to deviations of frequency beyond the acceptable range, resulting in undesirable load-shedding or even large-scale blackouts [3]. These frequency variations can be quantified by two parameters: the time derivative of the frequency, known as rate-of-change-of-frequency (RoCoF), and the minimum value of the frequency during the transient period, known as frequency nadir [3], [4], [5], [6], [7] which are shown in Fig. 1. To overcome this problem, researchers have proposed the concept of virtual inertia (VI) [4], [5], [9] which consists of the integration of an energy storage system (ESS) into the grid to emulate the synchronous generator behavior [10], [11] by grid-connected converters (GCCs), commonly called grid forming converters (GFM) [12], [13], [14], [15]. However, since GCCs with GFM control strategies are controlled as a voltage source, the direct control of the ac voltage without an inner current control loop may lead

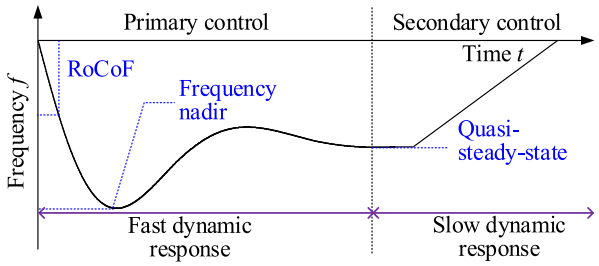

FIGURE 1. Transient response of grid frequency.

to difficulties in dealing with voltage drop faults, generating overcurrents and stability problems, making these solutions challenging to integrate into distribution grids [16].

Furthermore, most of the GFM strategies are intended for generation systems that consider large ESSs. The situation is quite different at the distribution level where the total cost is an important constraint. As an alternative, the distributed virtual inertia (DVI) concept was proposed in [9] and [17], which is based on several small contributions from individual GCCs through stored energy in dc bus capacitors. Since most GCCs at the distribution level are current-controlled converters, also known as grid following converters (GFL) [12], the GFL VI approach appears more suitable to supply DVI in distribution grids. However, since stored energy in dc-link capacitors is limited, the full frequency support including long-term frequency support requires an ESS with higher energy density.

Batteries have higher energy density compared to capacitors. Hence, since electric vehicles (EVs) remain plugged into the grid most of the day [1], EV batteries along with their bidirectional chargers (EVBCs) present a high potential to supply both VI and long-term frequency support. However, according to the state-of-the-art review, very few studies have been carried out to integrate VI support in EVBCs [1], [2], [18], [19], [20], [21], [22], [23], [24]. Moreover, the fast-dynamic response of active power required for VI implementation would decrease the battery lifetime [3]. To overcome this limitation, in [25] a hybrid energy storage system (HESS) is proposed. The dc-link capacitors supply the faster dynamic response for VI support, whereas the battery supplies the slower dynamic response for long-term frequency support. Moreover, the HESS is controlled through a nonisolated two-stage ac–dc converter composed of a bidirectional boost dc–dc converter cascaded to a voltage source inverter (VSI) implementing a GFM control strategy. Nevertheless, since typical EVBCs implement GFL control strategies and its power structure is based on a dual active bridge (DAB) dc–dc for galvanic isolation [26], [27], novel control strategies along with different procedures to size the dc-link capacitors should be developed to implement VI and long-term frequency support.

In this context, this article introduces a novel design and control approach for an isolated two-stage ac–dc converter intended for EVBCs, having the capability of managing an HESS to supply both, VI (fast response) and long-term frequency support (slow response). However, since dc-link capacitance could be increased to implement VI, the volume of the ac–dc converter could be increased also. Hence, the proposed control strategy is intended for off-board EVBCs or for stationary batteries grid-connected where the reduced volume is not a critical parameter [27].

Therefore, the main contributions of this work are as follows.

1) An enhanced GFL VI for practical implementation is introduced. In the proposed method, the dc-link capacitor is sized considering the maximum allowed extra power to deliver VI support, and the overshoot in estimated frequency by the phase-locked loop (PLL) is minimized.
2) A novel control strategy to manage a HESS through an isolated two-stage ac–dc converter is proposed, where dc-link capacitors supply the fast-active power response for VI, whereas EV battery covers the long-term frequency support with slower dynamics. Moreover, reactive power support and harmonics compensation are also implemented to cover full V2G support.

The rest of this article is organized as follows: Section II briefly explains the traditional GFL VI approach. Section III presents the practical limitations to implementing VI in two-stage ac–dc converters. Section IV presents the proposed control strategy to manage the HESS for frequency and voltage support. Section V presents the design of a reduced-scale 2.5 kW prototype. Section VI presents the experimental results. Section VII compares the proposed strategy with other works. Section VIII concludes this article.

II. FUNDAMENTALS OF GFL VI

The GFL VI concept is based on the dynamics of the swing equation which is given by (1), where $\frac{d}{dt}$ is the time derivative operator, Δf_{pu} is the instantaneous frequency deviation, Δp is the power difference between the generated power p_g and the load p_l whereas H is the inertia constant [8]. All these variables are in per-unit quantities

$$p_g - p_l = \Delta p = 2H\frac{d}{dt}\Delta f_{pu}. \tag{1}$$

It can be easily followed that for a certain variation of power, the inertia reduction in power systems leads to higher RoCoF and higher peak deviation of frequency (lower nadir). Hence, the concept of GLF VI [4], [5], [9] consists of the integration of an ESS for adding an extra power p_{support} to the system according to (2), where $\Delta f'_{pu}$ is the instantaneous frequency of the system

$$p_g - p_l + p_{\text{support}} = \Delta p + p_{\text{support}} = 2H\frac{d}{dt}\Delta f'_{pu} \tag{2}$$

$$p_{\text{support}} = -2H_V\frac{d}{dt}\Delta f'_{pu}. \tag{3}$$

Then, replacing (3) in (2), the frequency dynamics of the system including the VI is given by the following:

$$\Delta p = 2\left(H + H_V\right)\frac{d}{dt}\Delta f'_{pu} = 2H'\frac{d}{dt}\Delta f'_{pu}. \tag{4}$$

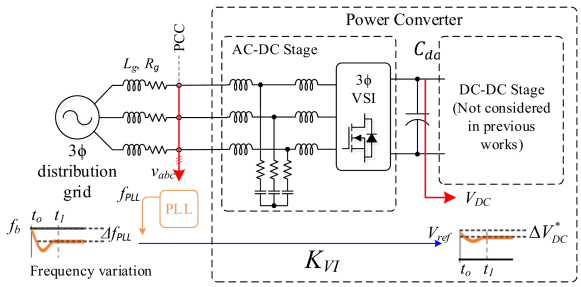

FIGURE 2. Traditional GFL VI implementation in a VSI.

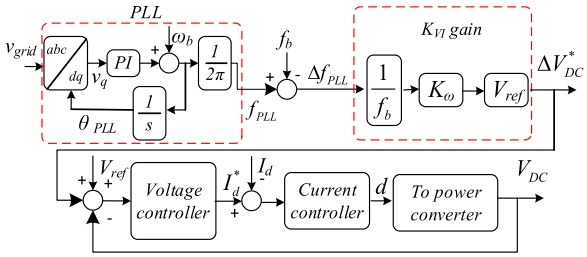

FIGURE 3. Typical GFL VI control strategy.

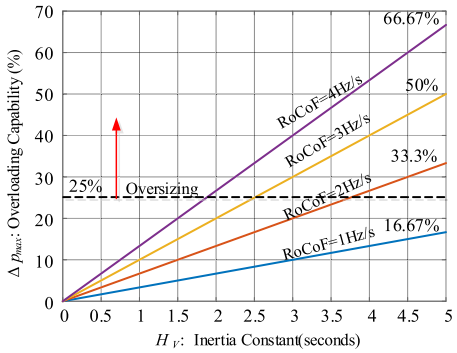

FIGURE 4. Oversizing for GFL VI implementation vs coefficients H_V.

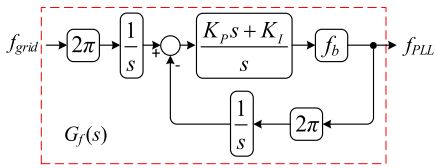

FIGURE 5. Frequency estimation dynamic by PLL.

This way, the effective inertia constant is increased to $H' = H + H_V$, increasing the frequency stability.

The implementation of GFL VI approach in a VSI was introduced in [9] according to the functional diagram presented in Fig. 2. Note that the GFL VI approach relates the frequency deviation Δf_{PLL}, measured by the PLL, with a voltage deviation ΔV_{DC} in the dc-link voltage, according to a gain K_ω. Moreover, the control strategy considers the well-known voltage and current control loops as presented in the block diagram of Fig. 3

Hence, a frequency deviation Δf_{PLL} generates a fast response of power through releasing/storing the energy in the dc-link capacitor C_{dc} according to a "virtual inertia" (H_V) coefficient given by (5), where H_c is defined in (6), being C_{DC} and V_{ref} the capacitance and the rated voltage of the dc-link, whereas P_o is the nominal power

$$H_V = K_\omega H_C \tag{5}$$

$$H_C = \frac{C_{\text{DC}} V_{\text{ref}}^2}{2P_o}. \tag{6}$$

The gain K_ω in (5) is designed for the allowed maximum frequency deviation $\Delta f_{\max}$ and a maximum voltage variation $\Delta V_{\text{DC\_max}}$ according to (7), where f_b and V_{ref} are the base grid frequency and the rated dc bus voltage, respectively

$$K_\omega = \frac{\Delta V_{\text{DC\_max}}}{\Delta f_{\max}} \frac{f_b}{V_{\text{ref}}}. \tag{7}$$

Then, the dynamic response of dc-link voltage is related to the fast power response ΔP_{DC} (inertia response) according to the following:

$$\Delta P_{\text{DC}}(s) \approx \frac{2H_V P_o}{f_b} \underbrace{s\Delta f_{\text{PLL}}(s)}_{\text{RoCoF}}. \tag{8}$$

III. PRACTICAL LIMITATIONS TO IMPLEMENT GFL VI

A. POWER CONSTRAINTS FOR VI SUPPLY

For a correct design of the converter, the extra power ΔP_{DC} for VI implementation must be considered as an overload. For instance, Fig. 4 shows the relation between overloading capability Δp_{DC}, RoCoF and different inertia values based on (8) and considering a base frequency of 60 Hz. Note that for a RoCoF of 2 Hz/s and an inertia contribution of $H_V \approx 3.75$ s, an overloading capability of 25% is required. Moreover, considering $H_V \approx 5$ s, as proposed in [9], for a RoCoF of 2 Hz/s, 33% of overloading capability is required. Whereas, for a RoCoF of 4 Hz/s and a $H_V = 5$ s, the required overload is 66%. Hence, GFL VI implementation supporting high values of inertia and faster RoCoF constraints requires oversizing the ac–dc converter, which will increase the size and price of EVBCs.

B. FREQUENCY MEASUREMENT FROM PLL

To analyze the influence of the PLL dynamic in VI power response, the block diagram of the frequency estimation of a typical second-order PLL, as shown in Fig. 5, is considered. Where f_b is the grid frequency, while K_P and K_I are, respectively, the proportional and integral gains of the PI controller.

Therefore, the closed loop $G_f(s)$ transfer function (TFs) for frequency estimation can be expressed by the following:

$$G_f(s) = \frac{f_{\text{PLL}}}{f_{\text{grid}}} = \frac{\omega_b K_P s + \omega_b K_I}{s^2 + \omega_b K_P s + \omega_b K_I}. \tag{9}$$

The controller gains are tuned following [28]. The K_P gain is calculated to achieve the desired bandwidth (ω_{bw}) and the integral gain is tuned at $K_I = K_P \frac{\omega_{\text{bw}}}{10}$. Then, with the evaluation $G_{fCL}(s)$ for a unit ramp $f_{\text{grid}}(s) = \frac{1}{s^2}$, the RoCoF is

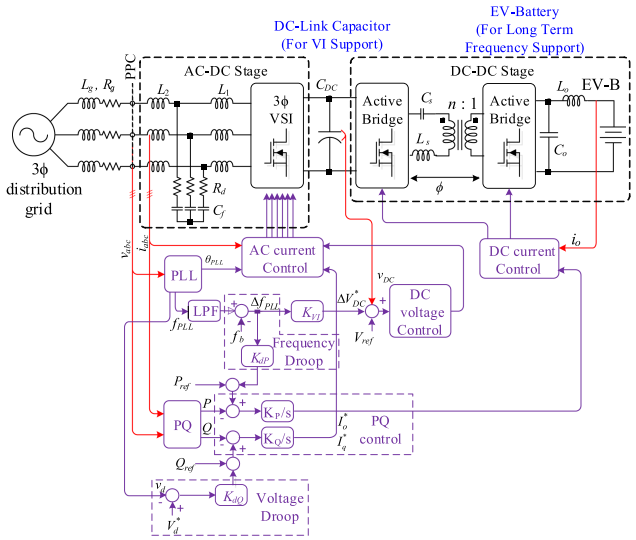

FIGURE 6. Block diagram of control strategy for V2G support in EVBCs.

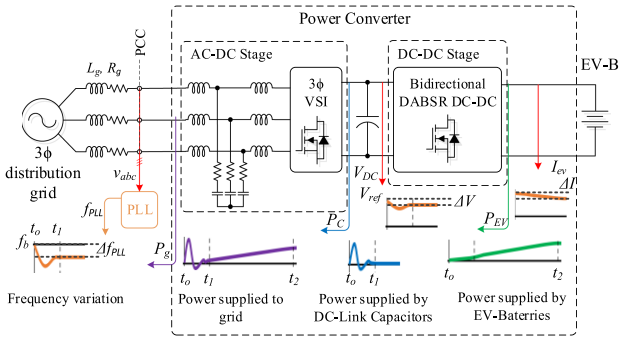

FIGURE 7. Block diagram of the proposed HESS management.

calculated according to the following:

$$\mathrm{RoCoF}\,(s) = s f_{\mathrm{PLL}}\,(s) = \frac{\omega_{\mathrm{bw}} s + 0.1{\omega_{\mathrm{bw}}}^2}{s^2 + \omega_{\mathrm{bw}} s + 0.1{\omega_{\mathrm{bw}}}^2}\frac{1}{s}. \quad (10)$$

Then, the maximum value of estimated RoCoF by PLL is 1.07 Hz/s. This means, an overshoot of 7% that, according to (8), increases the transient peak power supplied by the converter (ΔP_{DC}). To overcome the above-mentioned issues, an enhanced design procedure along with a novel control strategy to implement VI, long-term frequency support, reactive power support, and harmonics correction is introduced in the following sections.

IV. PROPOSED CONTROL STRATEGY

The block diagram of the proposed control strategy along with the scheme of the power stage are shown in Fig. 6. Note that a two-stage ac–dc topology is adopted which is composed of a three-phase VSI to interface with the grid, and a dual active bridge series resonant dc–dc converter to interface EV battery.

In the proposed control strategy, different V2G functionalities are implemented through managing an HESS. For this purpose, six controllers are designed: the ac current controller, the dc bus voltage controller, the dc current controller, the VI controller, the PQ controllers (active power P and reactive power Q controllers), and the droop controllers to compensate for frequency and voltage variations. In addition, a computational block to calculate active and reactive power (PQ block), a PLL, and transformation blocks complete the control strategy.

The management of HESS allows to decouple the dynamics responses of active power as shown in Fig. 7. Note that in front of a frequency variation increment Δf_{PLL}, the power delivered by the converter (P_g) is given by the following:

$$P_g = P_c + P_{\mathrm{EV}} \quad (11)$$

where P_c and P_{EV} are active powers supplied by the dc-link capacitors and the EV battery, respectively. The power P_c has a faster dynamic response compared to P_{EV}, and it is intended for VI support unlike P_{EV} which is focused on long-term frequency support. For simplicity, no power losses are considered. Moreover, in the proposed control strategy, the controllers are classified according to timescale as fast, medium, and slow response [24]. A fast response is required for the inner ac current controller on the ac–dc stage, with a timescale of around a few milliseconds. The medium response is related to dc-link voltage, VI, and dc current control, with a timescale of several milliseconds. Finally, the slow response corresponds to the PQ and droop controller with a timescale of several seconds. Since special care must be taken in choosing the bandwidth of medium response controllers to ensure system stability, the transfer functions, and controllers design are explained as follows.

A. FAST RESPONSE CONTROL: THE AC CURRENT CONTROLLER

For ac current, proportional + resonant controllers in the stationary $\alpha\beta$ frame are adopted. The TF from VSI voltage to ac current is given by (12) where L_1, L_2, C_f, and R_d are respectively the VSI side inductance, grid side inductance, filter capacitance, and damping resistance [29]

$$G_{iv} = \frac{i_\alpha\,(s)}{v_\alpha\,(s)} = \frac{R_d C_f s + 1}{C_f L_1 L_2 s^3 + R_d C_f\,(L_1 + L_2)\,s^2 + (L_1 + L_2)\,s}. \quad (12)$$

The transfer function of the PR controllers with selective harmonic GPR(s) is defined in (13), where Kp_c is the proportional gain, Kr_j (j=13,57,9) are the gains for resonant components, the term ξ is the damping factor which defines the bandwidth of the resonant components and the gain at each resonance frequency

$$G_{\mathrm{PR}}\,(s) = Kp_C + \sum_{j=1}^{n} \frac{Kr_j s}{s^2 + 2\xi\omega_0 s + {\omega_0}^2}. \quad (13)$$

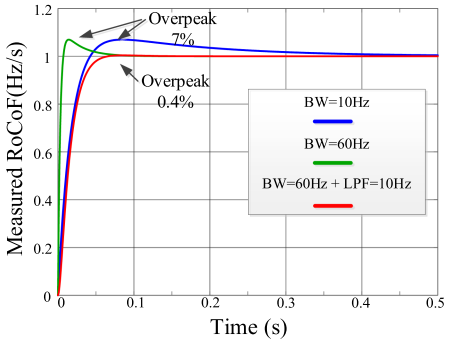

FIGURE 8. Measured RoCoF with three different PLL configurations.

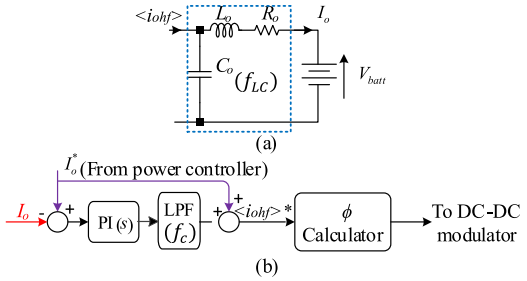

FIGURE 9. Battery current model. (a) Equivalent circuit. (b) Controller.

B. MEDIUM RESPONSE CONTROL

1) DC-LINK VOLTAGE CONTROLLER

The dc-link voltage controller is designed to provide the reference (I_{d_ref}) for ac current controller according to the following equation, where m is the modulation index

$$G_{vi}(s) = \frac{v_{DC}(s)}{i_d(s)} \approx m\frac{1}{C_{DC}s}. \tag{14}$$

Moreover, since the reference for the dc-link voltage ΔV_{DC}^* is provided by the VI controller, the dynamics of VI controller should be slower to ensure the system stability.

2) ENHANCED GFL VI CONTROLLER

As explained in Section III, the traditional GFL VI approach generates an overshoot of 7% in the frequency estimation by the PLL. To reduce the overshoot, the estimated frequency f_{PLL} is filtered by a first-order low-pass filter (LPF), as shown in Fig. 6. The LPF must be tuned with a cutoff frequency lower than the dc-link voltage dynamic response to ensure stability. To evaluate the effectiveness on the resulting overshoot, the PLL response was evaluated with three different configurations: a PLL tuned at 10 Hz bandwidth without LPF, a PLL tuned at 60 Hz bandwidth without LPF, and a PLL tuned at 60 Hz bandwidth with a LPF tuned at 10 Hz. The transient responses are depicted in Fig. 8. Note that PLL with LPF filter achieves an overshoot of just 0.4%. This value can be obtained by evaluating the PLL TF $G_f(s)$, given by (9), including the LPF TF, leading to the following:

$$\text{RoCoF}(s) = \frac{\omega_{bw}s + 0.1{\omega_{bw}}^2}{s^2 + \omega_{bw}s + 0.1{\omega_{bw}}^2}\frac{1}{s}\left(\frac{\frac{\omega_{bw}}{6}}{s + \frac{\omega_{bw}}{6}}\right). \tag{15}$$

With cutoff frequency of $\omega_{bw}/6$ for the LPF, following the procedure detailed Section III-B, a maximum RoCoF of 1.004 Hz/s is calculated. Hence, the overshoot in the estimated frequency has been considerably decreased, which leads lower transient peak deviation for both dc bus voltage and supplied power for VI.

3) BATTERY CURRENT CONTROLLER

The equivalent circuit to control battery current I_o is shown in Fig. 9(a), where L_o, C_o are the inductance and capacitance for the dc filter and R_o is the inductor series resistance, whereas the averaged current source $\langle i_{ohf}\rangle$ is given by the following [24]:

$$\langle i_{ohf}\rangle = \frac{8nV_{DC}}{\pi^2 Z\left(F - \frac{1}{F}\right)}\sin(\phi). \tag{16}$$

In (16), ϕ is the phase-shift angle, n is the turns-ratio of HF transformer, V_{DC} is the dc-link voltage, Z is the tank impedance, and F is the ratio between the switching frequency ω_s and the resonance frequency ω_r. The parameters Z, F, and ω_r are defined in (17), where L_s and C_s are the inductance and capacitance of the resonant circuit [24]

$$Z = \sqrt{\frac{L_s}{C_s}}\ ;\ F = \frac{\omega_s}{\omega_r}\ ;\ \omega_r = \frac{1}{\sqrt{L_sC_s}}. \tag{17}$$

Then, according to Fig. 9(a), the simplified TF for battery current (I_o) is given by the following equation, where ω_{LC} is the cutoff frequency of the L_o, C_o filter

$$G_i = \frac{I_o(s)}{\langle i_{ohf}\rangle(s)} = \frac{{\omega_{LC}}^2}{s^2 + \frac{R_o}{L_o}s + {\omega_{LC}}^2}. \tag{18}$$

The block diagram of the proposed dc current controller is shown in Fig. 9(b). The LPF is tuned at ω_c considering two decades lower than ω_{LC} to attenuate the resonance peak of $G_i(s)$. With this consideration, the loop-gain TF (T_i) can be approximated according to (19), where that $G_{io}(s)$ is considered as unity since $\omega_c \ll \omega_{LC}$. Then, the zero ω_i is tuned to eliminate the pole. Thus, the closed-loop TF $G_{iCL}(s)$ is given by (20)

$$G_{iOL} = \text{PI}(s)\,\text{LPF}(s)\,G_{io}(s) = k_p\left(\frac{s + \frac{1}{T_i}}{s}\right)\frac{\omega_c}{(s + \omega_c)} \tag{19}$$

$$G_{iCL} = \frac{G_{iOL}}{1 + G_{i\_OL}} = \frac{k_p\omega_c}{(s + k_p\omega_c)}. \tag{20}$$

C. SLOW RESPONSE CONTROLLERS

Instantaneous values of active power p and reactive power q are computed in the synchronous dq frame according to the following equations:

$$p = \frac{3}{2}(v_d i_d + v_q i_q) \tag{21}$$

TABLE 1. Parameters of the EVBC 2.5kW Prototype

Parameter	Variable	Value
Rated Power	$P_o \pm \Delta P_{max}$	2.5 kW±500W
Grid frequency	$f_b \pm \Delta f_{max}$	60 Hz ± 0.2 Hz
DC Link voltage	$V_{ref} \pm \Delta V_{DCmax}$	425 V ± 25V
Grid voltage	$V_m \pm \Delta V_m$	179 ± 17 Vp phase-n
Max. Considered RoCoF	$RoCoF_{max}$	3Hz/s
Battery voltage	V_b	400 V
DAB switching frequency	f_{sDC}	100 kHz
VSI switching frequency	f_{sAC}	48 kHz
LCL filter	L_1, L_2, C_f, R_d	900 µH, 250 µH, 15 µF, 2 Ω
Tank impedance	C_r, L_r	10.2 nF, 300 µH
Transformer turns ratio	n_t	1
Battery filter	L_o, C_o, R_o	300µH, 16uF, 0.2 Ω
DC Link Capacitance	C_{DC}	2.9mF

$$q = \frac{3}{2}\left(v_d i_q - v_q i_d\right). \tag{22}$$

Since v_q is tracked by PLL synchronization, $v_q \approx 0$ and $v_d \approx V_m$, where V_m is the amplitude of grid voltages. Therefore, TFs for p and q are given by the following:

$$G_{pq}(s) = \frac{p}{i_d}(s) = \frac{q}{i_q}(s) = \frac{3}{2}V_m. \tag{23}$$

Then, integral controllers with gains K_p, K_q are adopted (see Fig. 6) and the closed loop TFs G_{pcL}, G_{qcL} are given by the following:

$$G_{pcL}(s) = G_{qcL}(s) = \frac{1.5V_m K_p}{s + 1.5V_m K_p} = \frac{1.5V_m K_q}{s + 1.5V_m K_q}. \tag{24}$$

Finally, droop controllers are tuned through gains K_{dP} and K_{dQ}, according to the following equations:

$$P^* = P_{\text{ref}} + K_{dP}\Delta f_{\text{PLL}} \tag{25}$$

$$Q^* = Q_{\text{ref}} + K_{dQ}\left(V_d^* - v_d\right). \tag{26}$$

V. SYSTEM DESIGN

To validate the proposed control strategy, a 2.5 kW EVBC based on the parameters listed in Table 1 was evaluated.

For practical implementation, ΔV_{DCmax} is limited to ensure lineal modulation [9], whereas the dc-link capacitance is sized considering the maximum allowed extra power ΔP_{max} to VI support. Therefore, ΔP_{DC}, given by (8), must be limited to ΔP_{max}, according to the following equation:

$$\Delta P(s) \approx \frac{2H_V P_o}{f_b}\text{RoCoF}_{\text{max}} \quad \leq \Delta P_{\text{max}}. \tag{27}$$

Then, from (6), (7), and (27), the maximum allowable dc capacitance is calculated by the following:

$$C_{\text{DC}} \leq \frac{f_b \Delta P_{\text{max}}}{K_\omega V_{ref}^2 \text{RoCoF}_{\text{max}}}. \tag{28}$$

Since $\text{RoCoF}_{\text{max}}$ is a priori known value defined by grid codes, the gain K_ω, given by (7), is calculated as $K_\omega = 17.65$ from parameters of Table 1. Then, replacing values in (28), $C_{\text{DC}} \leq 3.13$ mF is calculated. With this consideration, $C_{\text{DC}} = 2.9$ mF is adopted. Then, according to (5) and (6), an inertia of $H_V \approx 1.85$ is obtained; thus, according to Fig. 4, the converter can provide VI in front of frequency variations up to 3 Hz/s without exceeding its limits.

TABLE 2. Bandwidths for the Controllers

Fast	Medium				Slow
AC Current	PLL	Bus DC	Frequency LPF	Battery Current	P &Q
800 Hz	60 Hz	30 Hz	10 Hz	5 Hz	1 Hz

TABLE 3. Controller Gains of the EVBC 2.5kW Prototype

Controller	Gains
AC Current	K_{pc}=5.3, K_{ic}=2668, K_{r3}=889, K_{r5}=533, K_{r7}=381, K_{r9}=296
Battery Current	K_{pbc}=1, K_{ibc}=31.416
PLL	K_{ppll}=1, K_{ipll}=37.7
DC-Link voltage	K_{pv}=0.6489, K_{iv}=4.8036
Inertia	K_{VI}=125
Droop	K_{dP}=2000, K_{dQ}=23.53
P-Q Controller	K_p=0.0234

On the other side, according to constraints detailed in Section IV, the chosen controller's bandwidths are listed in Table 2.

Note in Table 2 that the controllers are classified according to the dynamic response. The ac current controller is the fastest, whereas the active and reactive controllers (P&Q) are the slowest. Moreover, among the medium dynamic responses controllers, the PLL is tuned considering a bandwidth equal to the grid frequency [9] whereas, the DC-Link voltage controller has a bandwidth higher than the battery current and the LPF cascaded to the PLL, which allows to ensure the stability system [30].

Hence, considering the bandwidths of Table 2, the controller parameters are listed in Table 3. The PLL, dc-link voltage, and ac-current controller's parameters are tuned following the methodology of a grid connected converter [29]. The battery current and P&Q controllers' parameters are calculated according the first-order systems given by (20) and (24), respectively, and the desired bandwidth given in Table 3. Finally, the droop gains K_{dP} and K_{dQ} are calculated considering power deviations of $\Delta P_{\text{ref}} = 400$ W and $\Delta Q_{\text{ref}} = 400$ VAR for frequency and voltage variations of 0.2 Hz and 17 V, respectively [31].

The bode plot of the loop gain for current controller $T_i(s)$, given by (19), is shown in Fig. 10. Note that the crossover frequency (f_c) is much lower than the cutoff frequency (f_{LC}) of the L_oC_o filter. Hence, the resonance peak of $G_i(s)$, given by (18), is attenuated in −53 db.

VI. EXPERIMENTAL RESULTS

A 2.5 kW EVBC prototype was built as shown in Fig. 11, according to Table 1. The ac source Chroma 61702 was employed for testing grid frequency and voltage variations. Whereas the bidirectional dc power source Keysight RP7900 was employed to emulate the EV battery. The complete control strategy is implemented on a TMS320F28379D dual-core digital signal processor.

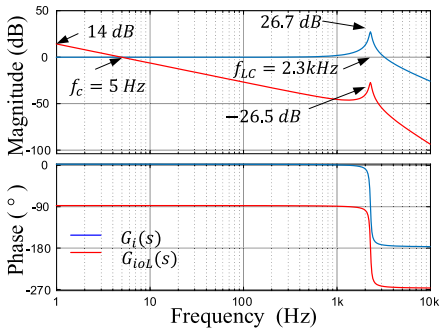

FIGURE 10. Bode plots of loop gain TF of battery current controller.

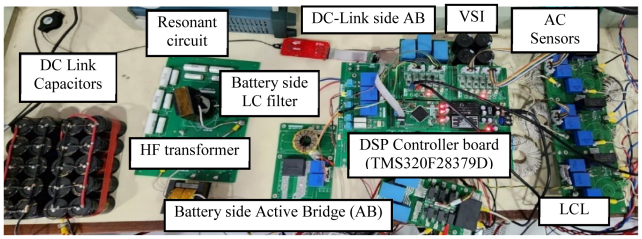

FIGURE 11. 2.5 kW EVBC prototype.

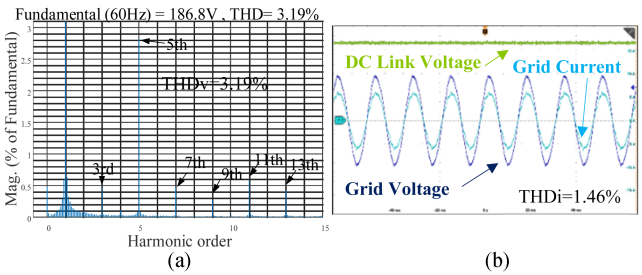

FIGURE 12. (a) Voltage spectrum. (b) Compensated grid current.

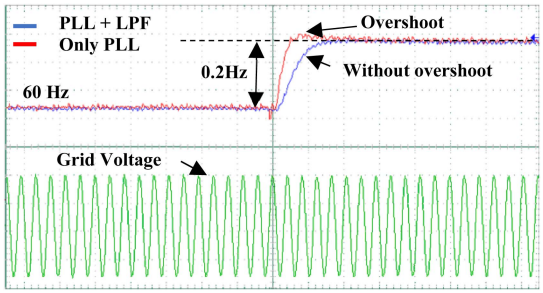

FIGURE 13. Dynamic response of the estimated frequency.

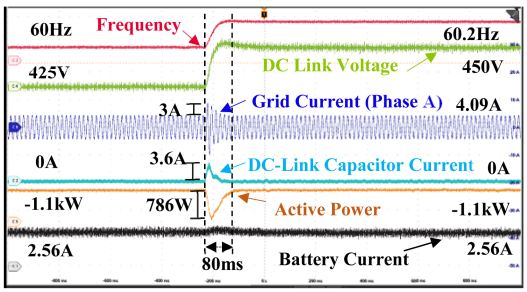

FIGURE 14. Waveforms for frequency variation of +0.2 Hz.

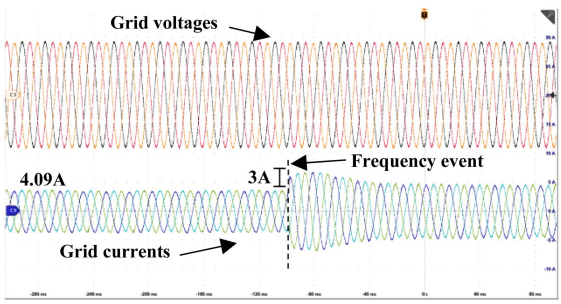

FIGURE 15. Waveforms of grid voltages and currents for a frequency variation of +0.2 Hz.

A. HARMONIC COMPENSATION

To test this functionality, the converter was connected to an ac grid with THDv = 3.19%. The corresponding voltage harmonic spectrum is presented in Fig. 12(a). The test was performed considering a load of 1.6 kW (64% of the rated power). The resulting ac is presented in Fig. 12(b). Note that the main harmonics components of grid voltage have been suppressed and the obtained THDi is only 1.46%.

B. ENHANCED VI RESPONSE

The dynamic response of the estimated frequency for a frequency step of 0.2 Hz is shown in Fig. 13. Two cases are analyzed to estimate the grid frequency: using only a PLL and using a PLL cascaded to a first-order LPF. The bandwidth of the PLL is 60 Hz, whereas for the LPF is 10 Hz respectively. Note that, filtering the estimated frequency by a LPF allows to decrease considerably the overshoot which validates the analytic and simulation results of the proposed method shown in Fig. 8.

The VI response was validated for "grid to vehicle" (G2V) mode, at 1.1 kW. For this test, the droop controllers were disabled. The results waveforms are shown in Figs. 14 and 15, respectively.

For a step-up frequency variation of +0.2 Hz, the measured RoCoF was 5.1 Hz/s. As frequency increases, dc voltage reference is increased proportionally to gain K_{VI} from 425 to 450 V. The dc-link capacitor current achieves a transient peak value of 3.6 A, increasing the grid currents in 3 A. The fast dynamic response of active power for VI support achieves a transient peak of 786 W, according to (8), returning to the steady state of −1.1 kW after 80 ms. Note that the current consumed by the battery remains almost constant in 2.56 A but presents a little variation caused by dc-link voltage change. The obtained results are coherent with the estimations, where VI support is supplied by the dc-link capacitors, maintaining the battery current almost constant.

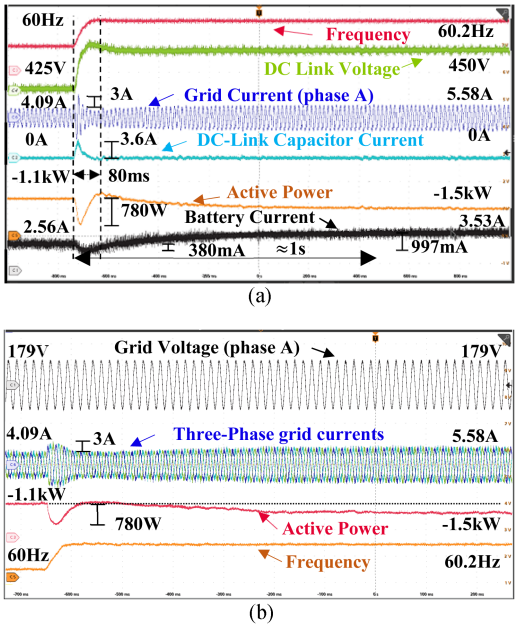

FIGURE 16. System response for a step of +0.2 Hz. (a) Main waveforms. (b) Ac currents.

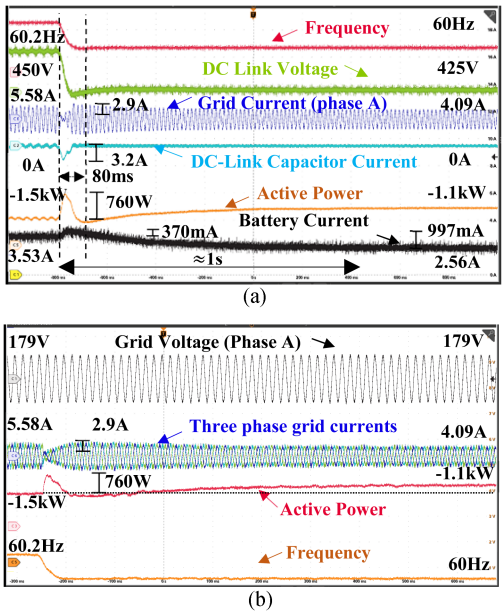

FIGURE 17. System response for a step of −0.2 Hz. (a) Main waveforms. (b) Ac currents.

C. HESS RESPONSE IN FRONT OF FREQUENCY STEPS

The full control strategy was verified by step frequency event of ±0.2 Hz in Figs. 16 and 17, respectively.

Note in Fig. 16 that initially the EVBC extracts 1.1 kW from the grid, working in G2V mode. The measured frequency by PLL is 60 Hz, the grid current peak value is 4.09 A, dc-link voltage takes its nominal value of 425 V, whereas the battery current is 2.56 A. Then, a frequency step of +0.2 Hz is applied. The VI response is validated by the transient demand of 780 W since the dc-link voltage increases from 425 to 450 V. Whereas the slower dynamic response for long-term frequency support is validated by the smooth variation from −1.1 to −1.5 kW. Note that the current of DC-Link capacitors achieves its steady state 80 ms after the frequency event, whereas the battery current achieves its steady state after almost 1s, which means 12.5 times slower than the VI controller response.

Next, a step of −0.2 Hz is applied, as shown in Fig. 17. The VI response is validated by the power transient of 760 W to decrease the dc-link voltage from 450 to 425 V. The slower dynamic response of active power is validated by the smooth variation of 400 W after 1 s. The results confirm that VI support is provided by dc-link capacitors whereas long-term frequency support with a slower dynamic is provided by batteries.

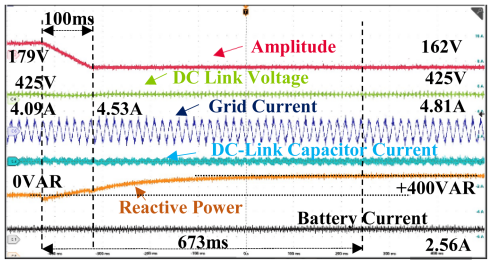

FIGURE 18. RPC response for an amplitude variation of −17 V.

D. VOLTAGE SUPPORT BY REACTIVE POWER

Main results of the voltage support in front a grid voltage amplitude reduction are presented in Fig. 18. Amplitude decreases linearly from 179 to 162 V (17 V) in 100 ms, producing a small decrease in the dc-link voltage, whereas the grid current increases from 4.09 to 4.53 A (peak).

According to the voltage droop controller, since reactive power increases from 0 to +400 VAR, the grid current increases from 4.53 to 4.81 A (peak) after almost 673 ms. Note that the battery current remains constant at 2.56 A. In contrast, the dc-link capacitor current is slightly increased to supply reactive power support, validating the proposed control strategy to manage the HESS.

VII. DISCUSSION

The proposed control strategy is briefly compared with similar studies implementing VI and with experimental results, which are shown in Table 4. Four comparison parameters were considered: Validated V2G functionalities, control strategy, power stage configuration, and adopted energy storage devices.

For the first parameter, validated V2G functionalities, note that, only for the proposed converter the full V2G functionalities, including VI, long-term frequency support, voltage support by reactive power compensation, and harmonics compensation have been validated.

TABLE 4. Comparison With Other Studies

Parameter	Proposed work	GFL works [9],[30]	GFM works [25]	Mixed GFM and GFL work [32]
Validated V2G Functionalities	VI, long-term frequency support, voltage support by reactive power, harmonic compensation	VI only	VI, Long-frequency support	VI, Long-term frequency support
Control Strategy	GFL	GFL	GFM	GFM for VI and GFL for long-term frequency support
Power Stage configuration	VSI cascaded to an isolated and bidirectional DAB DC-DC converter	VSI only	VSI cascaded to a non-isolated bidirectional Boost Converter	Two independent two-stage AC-DC converter composed of a VSI cascaded to a non-isolated bidirectional Boost Converter
Energy Storage Devices	HESS: DC-Link Capacitors + Battery	DC-Link Capacitors	HESS: DC-Link Capacitors + Battery	HESS: Supercapacitor + Battery

The second compared parameter was the control strategy. Since the proposed control strategy implements the GFL strategy then, it can be easily implemented in distribution grids because GFM inverters without an inner current control loop may lead to difficulties in dealing with voltage drop faults, generating over-currents and stability problems, making these solutions challenging to integrate into distribution grids [16].

The third compared parameter was the adopted power stage for ac–dc converter. The proposed converter uses a two-stage composed of VSI cascaded to an isolated and bidirectional DAB dc–dc converter. The proposed converter allows to obtain higher efficiency and reduced volume since the DAB converter operates on ZVS mode with higher switching frequency compared to structures used in other studies. Moreover, the proposed ac–dc structure can be used in off-board EV battery chargers since galvanic isolation is required, unlike other studies. On the other side, the proposed structure has more adaptability to interface to the battery with lower voltage, since the HF turns–ratio relationship can be modified according to the battery voltage, unlike the bidirectional boost converter which is limited in gain.

Finally, the fourth compared parameter was adopted energy storage devices. The use of an HESS is also proposed in [25] and [32] A similar idea of this work is proposed [25] but implementing a GFM control strategy and a non-isolated ac–dc converter. However, since the dc-link voltage is changed according to grid frequency variation, but it is defined by the battery, there is not a real power decoupling in the fast dynamic, which will reduce the battery lifetime. A different approach is implemented in [32] where two independent nonisolated ac–dc converters are used. The first ac–dc implements VI support by a GFM control strategy, whereas the second ac–dc implements the long-term frequency support by a GFL control strategy. Since two independent ac–dc converters are used, the price is considerably increased, unlike the proposed structure which implements full V2G functionalities in a unique ac–dc converter.

VIII. CONCLUSION

This work presents a novel control strategy that allows the operation of a two-stage ac–dc as a fully controllable HESS able to supply voltage and frequency support while ensuring high-quality in grid current. The proposed strategy ensures that the fast dynamic response of active power is supplied by the dc-link capacitors. Whereas the battery provides long-term-frequency support with a slower dynamic response. Hence, the VI implementation has no negative impact on the battery lifetime. Additional contributions are the practical considerations to GFL VI implementation and the minimization of the overshoot in frequency estimation by PLL. The proposed strategy can be implemented in existing ac–dc converters with only a firmware upgrade, being ideal for off-board EVBCs but also for stationary batteries in case frequency support is required to work permanently. Future works will be focused on implementing the full V2G functionalities but considering unbalanced grid voltages and weak grids.

REFERENCES

[1] Q. Hu, S. Bu, and V. Terzija, "Distributed P and Q provision-based voltage regulation scheme by incentivized EV fleet charging for resistive distribution networks," *IEEE Trans. Transp. Electrific.*, vol. 7, no. 4, pp. 2376–2389, Dec. 2021.

[2] M. Restrepo, J. Morris, M. Kazerani, and C. A. Cañizares, "Modeling and testing of a bidirectional smart charger for distribution system EV integration," *IEEE Trans. Smart Grid*, vol. 9, no. 1, pp. 152–162, Jan. 2018.

[3] J. Fang, H. Li, Y. Tang, and F. Blaabjerg, "On the inertia of future more-electronics power systems," *IEEE J. Emerg. Sel. Topics Power Electron.*, vol. 7, no. 4, pp. 2130–2146, Dec. 2019.

[4] U. Tamrakar, D. Shrestha, M. Maharjan, B. P. Bhattarai, T. M. Hansen, and R. Tonkoski, "Virtual inertia: Current trends and future directions," *Appl. Sci.*, vol. 7, no. 7, 2017, Art. no. 654.

[5] M. M. Hussein, T. Senjyu, M. Orabi, M. A. A. Wahab, and M. M. Hamada, "Control of a stand-alone variable speed wind energy supply system," *Appl. Sci.*, vol. 3, pp. 437–456, 2013.

[6] R. Yan, T. K. Saha, N. Modi, N.-A. Masood, and M. Mosadeghy, "The combined effects of high penetration of wind and PV on power system frequency response," *Appl. Energy*, vol. 145, pp. 320–330, 2015.

[7] B. K. Poolla, S. Bolognani, and F. Dörfler, "Optimal placement of virtual inertia in power grids," *IEEE Trans. Autom. Control*, vol. 62, no. 12, pp. 6209–6220, Dec. 2017.

[8] P. Kundur, *Power System Stability and Control*. New York, NY, USA: McGraw-Hill, 1994.

[9] J. Fang, H. Li, Y. Tang, and F. Blaabjerg, "Distributed power system virtual inertia implemented by grid-connected power converters," *IEEE Trans. Power Electron.*, vol. 33, no. 10, pp. 8488–8499, Oct. 2018.

[10] K. Y. Yap, C. R. Sarimuthu, and J. M. Y. Lim, "Virtual inertia-based inverters for mitigating frequency instability in grid-connected renewable energy system: A review," *Appl. Sci.*, vol. 9, no. 24, 2019, Art. no. 5300, doi: 10.3390/app9245300.

[11] B. Muftau and M. Fazeli, "The role of virtual synchronous machines in future power systems: A review and future trends," *Elect. Power Syst. Res.*, vol. 206, 2022, Art. no. 107775.

[12] W. Du et al., "Modeling of grid-forming and grid-following inverters for dynamic simulation of large-scale distribution systems," *IEEE Trans. Power Del.*, vol. 36, no. 4, pp. 2035–2045, Aug. 2021.

[13] P. Makolo, R. Zamora, and T. T. Lie, "The role of inertia for grid flexibility under high penetration of variable renewables - A review of challenges and solutions," *Renewable Sustain. Energy Rev.*, vol. 147, 2021, Art. no. 111223.
[14] Q.-C. Zhong and G. Weiss, "Synchronverters: Inverters that mimic synchronous generators," *IEEE Trans. Ind. Electron.*, vol. 58, no. 4, pp. 1259–1267, Apr. 2011.
[15] Q.-C. Zhong, P.-L. Nguyen, Z. Ma, and W. Sheng, "Self-synchronized synchronverters: Inverters without a dedicated synchronization unit," *IEEE Trans. Power Electron.*, vol. 29, no. 2, pp. 617–630, Feb. 2014.
[16] M. G. Taul, X. Wang, P. Davari, and F. Blaabjerg, "Current limiting control with enhanced dynamics of grid-forming converters during fault conditions," *IEEE J. Emerg. Sel. Topics Power Electron.*, vol. 8, no. 2, pp. 1062–1073, Jun. 2020.
[17] S. D'Arco, J. A. Suul, and O. B. Fosso, "A virtual synchronous machine implementation for distributed control of power converters in SmartGrids," *Elect. Power Syst. Res.*, vol. 122, pp. 180–197, 2015.
[18] A. Sharma and S. Sharma, "Review of power electronics in vehicle-to-grid systems," *J. Energy Storage*, vol. 21, pp. 337–361, 2019, doi: 10.1016/j.est.2018.11.022.
[19] M. C. Kisacikoglu, M. Kesler, and L. M. Tolbert, "Single-phase on-board bidirectional PEV charger for V2G reactive power operation," *IEEE Trans. Smart Grid*, vol. 6, no. 2, pp. 767–775, Mar. 2015.
[20] K. Kaur, M. Singh, and N. Kumar, "Multiobjective optimization for frequency support using electric vehicles: An aggregator-based hierarchical control mechanism," *IEEE Syst. J.*, vol. 13, no. 1, pp. 771–782, Mar. 2019.
[21] S.-A. Amamra and J. Marco, "Vehicle-to-grid aggregator to support power grid and reduce electric vehicle charging cost," *IEEE Access*, vol. 7, pp. 178528–178538, 2019.
[22] J. A. Suul, S. D'Arco, and G. Guidi, "Virtual synchronous machine-based control of a single-phase bi-directional battery charger for providing vehicle-to-grid services," *IEEE Trans. Ind. Appl.*, vol. 52, no. 4, pp. 3234–3244, Jul./Aug. 2016.
[23] A. Kazemtarghi, S. Dey, and A. Mallik, "Optimal utilization of bidirectional EVs for grid frequency support in power systems," *IEEE Trans. Power Del.*, vol. 38, no. 2, pp. 998–1010, Apr. 2023.
[24] D. Sal y Rosas and A. Zarate, "Single-phase grid-forming strategy with power decoupling implementation for electrolytic-capacitor-free EV smart battery charger," *Energies*, vol. 16, no. 2, 2023, Art. no. 894.
[25] J. Fang, Y. Tang, H. Li, and X. Li, "A battery/ultracapacitor hybrid energy storage system for implementing the power management of virtual synchronous generators," *IEEE Trans. Power Electron.*, vol. 33, no. 4, pp. 2820–2824, Apr. 2018.
[26] J. Yuan, L. Dorn-Gomba, A. D. Callegaro, J. Reimers, and A. Emadi, "A review of bidirectional on-board chargers for electric vehicles," *IEEE Access*, vol. 9, pp. 51501–51518, 2021.
[27] H. Wouters and W. Martinez, "Bidirectional on-board chargers for electric vehicles: State-of-the-art and future trends," *IEEE Trans. Power Electron.*, vol. 39, no. 1, pp. 693–716, Jan. 2024.
[28] D. G. Holmes, T. A. Lipo, B. P. McGrath, and W. Y. Kong, "Optimized design of stationary frame three phase AC current regulators," *IEEE Trans. Power Electron.*, vol. 24, no. 11, pp. 2417–2426, Nov. 2009.
[29] J. C. U. Peña, L. P. Sampaio, M. A. G. de Brito, and C. A. Canesin, "RLC passive damped LCL single-phase voltage source inverter with capability to operate in grid-connected and islanded modes: Design and control strategy," *Elect. Eng.*, vol. 102, pp. 2509–2519, 2020.
[30] Q. Peng, J. Fang, Y. Yang, T. Liu, and F. Blaabjerg, "Maximum virtual inertia from DC-link capacitors considering system stability at voltage control timescale," *IEEE J. Emerg. Sel. Topics Circuits Syst.*, vol. 11, no. 1, pp. 79–89, Mar. 2021.
[31] *IEEE Standard for Interconnecting Distributed Resources with Electric Power Systems*, in *IEEE Std 1547a-2014*, pp. 1–16, May 21, 2014, doi: 10.1109/IEEESTD.2014.6818982.
[32] C. Sun, S. Q. Ali, G. Joos, and F. Bouffard, "Design of hybrid-storage-based virtual synchronous machine with energy recovery control considering energy consumed in inertial and damping support," *IEEE Trans. Power Electron.*, vol. 37, no. 3, pp. 2648–2666, Mar. 2022.

JHONATAN D. PAUCARA was born in 1992 in Peru. He received the B.S. degree in electronic engineering from the National University of Engineering, Lima, Peru, in 2013, and the M.S. degree in control engineering from PUCP University, San Miguel, Peru, in 2017. He is currently working toward the doctoral degree in energy engineering in the National University of Engineering.

His main research interests include the power electronics for microgrids and vehicle-to-grid.

JOSÉ CARLOS U. PEÑA was born in 1984 in Peru. He received the B.S. degree in electronic engineering from the National University of Engineering, Lima, Peru, in 2009, and the M.S. and Ph.D. degrees in electrical engineering from São Paulo State University, São Paulo, Brazil, in 2012 and 2016, respectively.

Since 2022, he has been a Researcher with the School of Electrical and Computer Engineering, University of Campinas. His research interests include power electronics, microgrids, and power quality.

DAMIAN SAL Y ROSAS was born on 1981 in Peru. He received the B.S. degree in electronic engineering from the National University of Engineering, Lima, Peru, in 2005, the M.S. degree in embedded systems from the ESIEE-Paris, Noisy-le-Grand, France, in 2009, and the Ph.D. degree in electrical engineering from Grenoble Alpes University, Grenoble, France, in 2017.

From 2011 to 2023, he worked as an Associate Professor with the National University of Engineering, where he was the Power Electronics research group chief. He is currently an Associate Professor with the University of Toulouse, UT3, Toulouse, France, working in the LAAS-CNRS Laboratory. His research interests include highly efficient power electronic converters for microgrid and electromobility applications.